HiSST: 4th International Conference on High-Speed Vehicle Science Technology
22 -26 September 2025, Tours, France

Large Eddy Simulation of Ramjet to Scramjet Transition

Christer Fureby[1]

Abstract

The dual-mode ramjet engine is a key candidate for hypersonic propulsion due to its ability to operate across a wide Mach number range. It requires a turbojet for low-speed operations (Ma≲2), while functioning as a thermally choked ramjet at moderate speeds (Ma≈3 to 4) and as a scramjet at high speeds (Ma≈5 to 8). Transitions between these modes are critical: the turbojet-to-ramjet shift is relatively controllable, but the ramjet-to-scramjet transition is complex and governed by aerothermodynamics. This study uses Large Eddy Simulations (LES) to support experimental work by Fotia & Driscoll, aiming to deepen understanding of this transition. The simulations show good agreement with experimental data and reveal detailed insights into flow behaviour and flame stabilization mechanisms during the ramjet to scramjet mode shift.

Keywords: ramjet to scramjet transition, large eddy simulation

1. Introduction

The need to realize new commercial flight routes combined with the desire to shorten the time of long-haul intercontinental or antipodal flights has recently boosted the interest in civil hypersonic flight vehicles. The feasibility of civil hypersonic flight poses an abundance of technical, environmental, human, and economic factors that have to be considered. Among the most critical aspects is the engine and its integration into the flight vehicle. Only a limited number of engine technologies appears suitable for civil hypersonic flight, and the most promising among these appears to be a combined cycle propulsion plant consisting of multiple turbojet engines combined with a dual mode ramjet engine. At present, a dual mode ramjet engine is envisioned to consist of an air-intake followed by an isolator, a combustor that may contain some flame holding mechanism, and finally an expansion nozzle with a duct to accommodate the exhaust from the turbojet engines, [1].

Designing such engine systems provides a grand challenge involving both turbojet, ramjet, and scramjet operation. The biggest challenges are likely the transition stages between turbojet and ramjet mode, and between ramjet and scramjet mode. Dual mode ramjet is still an emerging technology, and the participating flow and combustion physics, in particular during the transition stages, needs to be further investigated. This necessitates advanced joint experimental and computational studies that can provide temporally, spatially, and spectrally well-resolved data suitable for advanced analysis in order to build the understanding and answer the open questions.

In the combined cycle engine system, the turbojet engine(s) are operated for take-off, landing and low-speed manoeuvring, typically at flight Mach numbers Ma≲2. For higher flight speeds the dual mode ramjet engine will be gradually activated in a first transitional phase whereby the flight vehicle is accelerated to Ma≈3. At this point the dual mode ramjet engine will operate in thermally choked ramjet mode. Here, an isolator shock-train decelerates the flow to subsonic speed before fuel injection. A thermal throat then allows the exhaust to be accelerated back to supersonic speed. To reach higher flight speeds, 5≲Ma≲8, the engine will need to transition from the thermally choked ramjet mode to scramjet mode, requiring the shock-train in the isolator to gradually weaken until the flow is completely supersonic at the isolator exit and throughout the combustor.

[1] *Lund University, Div. of Heat Transfer, Lund, PO Box 118, SE 221-00, christer.fureby@energy.lth.se*

The aerodynamics and thermodynamics involved in ramjet and scramjet operation is extremely challenging, [2-4], and especially for the transitions from turbojet to ramjet, [5], and from ramjet to scramjet, [6]. A dual mode ramjet has no moving parts, and the ambient air is compressed and accelerated by the ram effect, [7]. Air enters the inlet and continues through the isolator section which acts as a compressor. The amount of compression hence increases with vehicle speed which is why a Ma number of at least 2 is needed for the engine to operate. Fuel is injected at the end of the isolator. This mixture ignites and burns in the downstream combustor, often using a flameholder to stabilize the flame, and the combustion products then expands in the nozzle.

One of the major obstacles to achieve functional dual mode ramjet combustion is the aerothermodynamics of the transition between ramjet and scramjet operation which is currently not well understood and is challenging to investigate. Because thrust strongly depends on compression, the ramjet needs high forward velocity to start the cycle, and for low speeds a turbojet engine discharging in a common nozzle is a good option. The transition between turbojet operation and ramjet operation is also challenging but can possibly be managed by throttling.

In this study we will investigate the transition from ramjet operation to scramjet operation using high fidelity numerical simulations based on Large Eddy Simulation (LES), [8], of a dual-mode combustor experiment in direct connect facility at the University of Michigan, [9-10]. In this experiment the transition is investigated by reducing the fuel equivalence ratio in steps to resemble the transition which is otherwise achieved by gradually increasing flow speed at fixed equivalence ratio. In Section 2 we briefly discuss the two different mode transitions and in Section 3 we discuss the experiments of Driscoll & Fotia, [9-10]. In Sections 4 and 5 we present the simulation model and the combustion reaction mechanisms used, whereas in Section 6 we discuss the simulation results and compare with experimental results. Finally, in Section 7 we provide some concluding remarks.

2. Mode Transitions in Dual Mode Ramjets

Figure 1 shows a schematic of the different operational modes of a combined turbojet and dual mode ramjet engine. As indicated in Section 1 the engine system operates in the turbine mode from take-off to about Ma 2, in the transitional and pure ramjet mode from Ma 2 to 5, and in the transitional and pure scramjet mode from Ma 5 to 8.

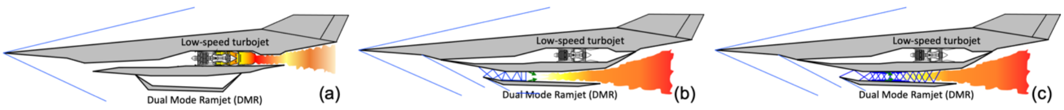

Fig. 1. Schematic of the turbine-based, ramjet and scramjet operational modes. (a) turbine mode, (b) ramjet mode and (c) scramjet mode.

Turbojet to ramjet transition is essential for the operation of turbine-based combined cycle engines, but it has rarely been investigated to the best of the authors' knowledge. Liu *et al.*, [11], however performed combined wind tunnel tests and numerical simulations to examine the method of smooth inlet mode transition and acquire additional inlet flow details. The mean pressure distribution was recorded in the experiment for validation and to evaluate the inlet performance. Combined experimental data and numerical simulation results suggest that smooth inlet mode transition can be achieved by keeping the total throttle ratio of the turbine engine constant, ensuring that the terminal shock wave is located near the throat of the inlet during the mode transition.

The ramjet to scramjet transition is a crucial and challenging phenomenon for dual mode ramjet engines, and it occurs during the ascent phase of a hypersonic vehicle. In the ramjet mode, a normal shock wave is generated due to the thermally choked downstream conditions, and the isolator shock-train train can consist of a series of nearly normal shocks. In the scramjet mode, on the other hand, the blockage because of combustion and fuel injection is small, the strong shock waves disappear, and the flow velocity remain supersonic throughout the combustor. The fuel feeding has a great impact on the ramjet to scramjet mode transition process, [12]. Micka & Driscoll, [13], have observed two distinct cavity stabilized combustion modes for ramjet operation, jet-wake stabilized, and cavity stabilized, whereas only the cavity stabilized mode is observed for scramjet operation. Wang *et al.*, [14], provide a review on the cavity-stabilized combustion for scramjet applications, and subjects like cavity-coupled fuel injection, flow and combustion coupling, optimal cavity geometry and scale, auto-ignition and flame propagation interactions, and unsteady effects have been widely discussed.

Ramjet to scramjet transition has been experimentally investigated by Fotia & Driscoll, [9-10], using pressure measurements and high-speed laser interferometry, and here it should be noted that the ramjet to scramjet transition can be achieved by adjusting two parameters, namely the equivalence ratio, ϕ, and the wall temperature, T_w. At the same time, they found that the ramjet to scramjet transition can be triggered through active fuel actuation and passive wall-heating.

3. The Driscoll & Fotia Direct Connect Facility Experiments

The Fotia & Driscoll, [15-16], direct connect facility experiments, figure 2, offers an exclusive opportunity to investigate the transition from ramjet to scramjet operation, and at the same time further validate models, like the LES model in [17-18]. A constant-area isolator is fed by a two-dimensional Ma 2.2 nozzle, and hydrogen is injected at the end of the isolator through a 2.49 mm diameter injector on the centreline, 44.5 mm upstream of the leading edge of a full-width cavity with a slanted downstream wall. A 4° diverging combustor section starts after the cavity and ultimately discharges into a large-diameter exhaust. An electric heater combined with a hydrogen fuelled vitiator was used to obtain air stagnation-temperatures between T_0=1040 K and 1500 K at stagnation pressures between p_0=420 kPa to 590 kPa. For the transition studies T_0 and p_0 were fixed at 1400 K and 448.2 kPa, respectively. Table 1 summarize the operating conditions considered for the ramjet to scramjet experiments in [15-16], through which the transition is facilitated by varying the H_2 inflow, resulting in global equivalence ratios ranging between ϕ=0.34 (ramjet mode) and 0.19 (scramjet mode).

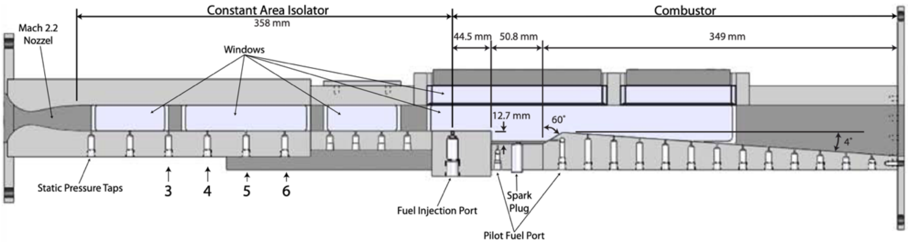

Fig. 2. Schematic of the University of Michigan dual mode combustor experiment the full length of which is considered in the present study.

Table 1. Operating conditions for the Fotia & Driscoll cases, [15-16].

Case	*Fuel*	T_0 *[K]*	p_0 *[kPa]*	ϕ	*Observed combustion mode*
F1	H_2	1400	448.2	0.34	ramjet
F3	H_2	1400	448.2	0.26	transitional
F5	H_2	1400	448.2	0.19	scramjet

The computational set-up starts at the Laval nozzle and ends at the exit of the combustor sec-tion. Hexahedral grids with ~11 and ~85 million cells, having refinement at the walls and in the cavity, are used. The LES Index of Quality, [19], show that 87% and 94% of the kinetic energy was resolved, respectively, rendering both grids appropriate for LES. Dirichlet boundary conditions are used for all variables at the inlet, and at the sonic injectors. At the outlet, Neumann conditions are used for all variables as the combustor dumps in a large exhaust. In the combustor, a no-slip LES subgrid wall-model, [20], is used for velocity together with zero Neumann conditions for all other variables.

4. Physical Models and Numerical Methods

The computational approach adopted is based on LES, and in section 4.1 we present the LES methodlogy followed in sections 4.2, 4.3 and 4.4 by explanations of the subgrid turbulence modelling, the turbulence chemistry interaction modelling, and the numerical methods, respectively.

4.1. The Large Eddy Simulation Methodology

Large Eddy Simulation (LES) of reactive flows, [8, 21-22], is based on the low-pass filtered equations of mass, momentum, and energy. The low-pass filtering is used to separate the resolved flow (denoted by tildes and overbars, depending on the use of density weighted filtering) from the unresolved (subgrid scale) flow. Filtering implies that only the physics associated with scales larger than the filter width, Δ, is explicitly resolved while the effect of smaller scales is estimated by subgrid models. Here, implicit filtering is used, resulting in that Δ is the grid spacing. For a viscous reacting mixture of N species with Fourier heat conduction and Fickian diffusion the LES equations are,

$$\begin{cases} \partial_t(\bar{\rho}) + \nabla\cdot(\bar{\rho}\tilde{\boldsymbol{v}}) = 0 \\ \partial_t(\bar{\rho}\tilde{Y}_i) + \nabla\cdot(\bar{\rho}\tilde{\boldsymbol{v}}\tilde{Y}_i) = \nabla\cdot(\tilde{\boldsymbol{j}}_i - \boldsymbol{b}_i) + \bar{\dot{w}}_i \\ \partial_t(\bar{\rho}\tilde{\boldsymbol{v}}) + \nabla\cdot(\bar{\rho}\tilde{\boldsymbol{v}}\otimes\tilde{\boldsymbol{v}}) = -\nabla\tilde{p} + \nabla\cdot(\tilde{\boldsymbol{S}} - \tilde{\boldsymbol{B}}) \\ \partial_t(\bar{\rho}\tilde{E}) + \nabla\cdot(\bar{\rho}\tilde{\boldsymbol{v}}\tilde{E}) = \nabla\cdot\left(-\tilde{p}\tilde{\boldsymbol{v}} + \tilde{\boldsymbol{S}}\tilde{\boldsymbol{v}} + \tilde{\boldsymbol{h}} + \Sigma_{i=1}^{N}(h_{i,f}^{\theta}\tilde{\boldsymbol{j}}_i) - \boldsymbol{b}_E\right) + \Sigma_{i=1}^{N}(\bar{\dot{w}}_i h_{i,f}^{\theta}) \end{cases} \quad (1)$$

Here, ρ is the density, $\boldsymbol{v}$ the velocity, Y_i the species mass-fractions, $\boldsymbol{j}_i \approx D_i\nabla Y_i$ the species mass flux vectors, D_i the species diffusivities, $\boldsymbol{b}_i = \bar{\rho}(\widetilde{\boldsymbol{v}Y_i} - \tilde{\boldsymbol{v}}\tilde{Y}_i)$ the species subgrid fluxes, $\dot{w}_i = P_{ij}\dot{w}_j$ the species formation rates, P_{ij} the stoichiometric matrix and $\dot{w}_j$ the reaction rates. In the momentum equation (1_3), $p = \rho RT$ is the pressure, R the specific gas constant, T the temperature, $\boldsymbol{S} = 2\mu\boldsymbol{D}_{\mathrm{D}}$ the viscous stress tensor, μ the viscosity obtained from Sutherland's formula, $\boldsymbol{D}_{\mathrm{D}}$ the deviatoric part of the rate of strain tensor and $\boldsymbol{B} = \bar{\rho}(\widetilde{\boldsymbol{v}\otimes\boldsymbol{v}} - \tilde{\boldsymbol{v}}\otimes\tilde{\boldsymbol{v}})$ the subgrid stress tensor. In the energy equation (1_4) the energy variable is the total sensible energy $E = \sum_{i=1}^{N}\left(Y_i\int_{T_0}^{T} C_{p,i}dT\right) - p/\rho + v^2/2$ being the sum of the sensible enthalpy and the kinetic energy. In addition, $p\boldsymbol{v}$ is the pressure work, $\boldsymbol{S}\boldsymbol{v}$ the viscous work, $\boldsymbol{h} = \kappa\nabla T$ the heat flux vector, κ the thermal diffusivity, $\sum_{i=1}^{N}(\dot{w}_i h_{i,f}^{\theta})$ the chemically heat release, and finally $\boldsymbol{b}_E = \bar{\rho}(\widetilde{\boldsymbol{v}E} - \tilde{\boldsymbol{v}}\tilde{E}) + (\overline{p\boldsymbol{v}} - \tilde{p}\tilde{\boldsymbol{v}}) - (\overline{\boldsymbol{S}\boldsymbol{v}} - \tilde{\boldsymbol{S}}\tilde{\boldsymbol{v}})$ the subgrid energy flux vector. D_i and κ are obtained from the viscosity using constant Schmidt, Sc_i, and Prandtl, Pr, numbers, [23].

4.2. LES Subgrid Flow Modeling

The subgrid stress tensor and flux vectors, or the unresolved transport terms, $\boldsymbol{B}$, $\boldsymbol{b}_E$ and $\boldsymbol{b}_i$, in the filtered transport equations (1) can be closed using many different models. Sagaut, [24], provides a comprehensive review of subgrid models for non-reactive and incompressible flows. Most often are these models extended to compressible and reactive flows using dimensional arguments. This can be disputed but in absence of experimental or direct numerical simulation data this constitutes today's standards. Following e.g. Li *et al.*, [25], the subgrid stress tensor can be represented, to first order, by the expression $\boldsymbol{B} \approx 2/3\bar{\rho}k\boldsymbol{I} - 2\mu_k\tilde{\boldsymbol{D}}_D$, in which k is the subgrid kinetic energy and μ_k the subgrid viscosity. A wide range of such subgrid viscosity models are available, [24, 26-29], including the Smagorinsky (SMG) model, [26], the Wall Adapting Local Eddy viscosity (WALE) model, [27], and the Hyper-viscosity model (HV), [28]. Here we use the Localized Dynamic k-equation Model (LDKM), [29], in which $\mu_k = c_k\bar{\rho}\Delta\sqrt{k}$, with k satisfying the modeled transport equation, $\partial_t(\bar{\rho}k) + \nabla\cdot(\bar{\rho}k\tilde{\boldsymbol{v}}) = -\boldsymbol{B}\cdot\tilde{\boldsymbol{D}} + \nabla\cdot(\mu_k\nabla k) - c_\varepsilon\bar{\rho}k^{3/2}/\Delta$, where the coefficients c_k and c_ε are evaluated dynamically using scale similarity. Based on earlier studies of high-speed flows, e.g. [30], involving comparison of Schlieren images, velocity, and velocity rms fluctuations, it is clear that LDKM performs better than other subgrid models, in particular with respect to capturing shock-trains, mixing and shock-boundary layer interactions. The subgrid flux vectors in the species and energy equations are modelled as $\boldsymbol{b}_E = (\mu/\mathrm{Pr}_t)\nabla E$ and $\boldsymbol{b}_i = (\mu/\mathrm{Sc}_t)\nabla Y_i$, in which $\mathrm{Pr}_t = 0.7$ and $\mathrm{Sc}_t = 0.85$ are the turbulent Prandtl and Schmidt numbers.

4.3. LES Combustion Modelling

The filtered formation rates in the species equations, $\overline{\dot{w}_i} = M_i P_{ij}\overline{\dot{w}_j}$, require separate treatment because of the strongly non-linear dependence on the subgrid distribution of temperature and concentration, as well as short time scales over which the rates can change. The large number of terms involved for large reaction mechanisms also increases the computational cost associated with the formation rates. Several methods to model the filtered formation rates exist and are typically divided into two classes. *Flamelet models* assume that the region of combustion is a thin layer with a small thickness compared with the length scales of the flow and that this layer preserves the internal structure of a one-dimensional diffusion flame, [31], or premixed flame, [32], which allow for pre-tabulation of the rates. *Finite Rate Chemistry (FRC) models* are instead based directly on solving the species transport equations (1_2) and using closure models for the filtered species formation rates which are allowed to depend freely on all species in the reaction mechanism, ensuring that the entire space of allowed states remain accessible without restricting to predefined flame structure, [22].

For a multi-step reaction mechanism, the filtered reaction rates are non-linear functions of the temperature, T, and species concentrations, C_i, $\overline{\dot{w}_j} = k_{f,j}\Pi_{i=1}^{N}C_i^{P_{ij}} - k_{b,j}\Pi_{i=1}^{N}C_i^{P_{ij}}$. Here, $k_{f,j}$ and $k_{b,j}$ are the forward and backward rates of reaction j as specified by the reaction mechanism, and $C_i = \rho Y_i/M_i$ are the species concentrations. Depending on the size of the reaction mechanism the complexity and non-linearities of the filtered formation rates increases, and due to these non-linearities the range of flow scales widens to also encompass the flame scales.

A collection of closure models for (2) suitable for multi-step reaction mechanisms have developed but it is not until recently we have had the computational resources to accurately evaluate these models *a priori* and *a posteriori*. In the Thickened Flame Model (TFM), [33], the flame is thickened so that it can be resolved on the grid whilst keeping the laminar flame speed, s_u, constant. In the Eddy Dissipation Concept (EDC) model, [34], Partially Stirred Reactor (PaSR) model, [35], and Fractal Model (FM), [36], the flow is considered to consist of turbulent fine structures of tube-, ribbon- or sheet-like geometries, comprising most of the viscous dissipation and molecular mixing, embedded in a weaker background, [37-38]. The EDC, PaSR, and FM use different approximations to estimate the reacting volume fraction, γ^*, such that $\overline{\dot{w}_i(C_i,T)} \approx \gamma^* \dot{w}_i(\tilde{C}_i,\tilde{T})$. The Eulerian Stochastic Fields (ESF) model [39] is a stochastic approach within the probability density function (PDF) class of combustion models [40]. An even more advanced model in the Linear Eddy Model (LEM) of Menon *et al.*, [41], in which the advection-diffusion-reaction coupling are fully resolved using a one-dimensional representation of turbulent advection, with the latter represented by the 'triplet map' that attempts to represent the effect of an eddy-turnover on property profiles along a notional line of sight.

Based on a comprehensive study of different LES combustion models for different low- and high-speed combustion applications, e.g. [18, 34, 42-44], we here use the PaSR model, [35]. Based on data from [45] together with a state-space analysis, we model the filtered formation rates as $\overline{\dot{w}_i} \approx \gamma^* \dot{w}_i(\tilde{C}_i,\tilde{T})$, in which the reacting volume fraction is $\gamma^* = \tau_c/(\tau^* + \tau_c)$, where τ^* is a mixing timescale and τ_c a chemical timescale. The chemical time scale can be modelled as $\tau_c \approx \delta_u/s_u$, where δ_u is the laminar flame thickness, whereas the mixing time scale is modelled as $\tau^* = \sqrt{\tau_\Delta \tau_K}$. Here, $\tau_\Delta = \Delta/v'$ is the resolved mixing time scale and $\tau_K = \sqrt{\nu/\varepsilon}$, where ε is the dissipation of k, is the Kolmogorov time scale.

4.4. Numerical Methods for High-Speed Flows

Numerical methods for LES of high-speed combustion with shocks, contact discontinuities and rarefaction waves are both important and challenging. Finite Volume Methods (FVM) prevails in fluid dynamics, at least for practical geometries. A specific requirement to resolve as much of the turbulence as possible ai low-dissipation schemes. These schemes are, however, poorly suited to capture shocks and other flow discontinuities, and to circumvent this, methodologies such as artificial dissipation and diffusion techniques, [46], or hybrid schemes, [47], have been developed.

The numerical method employed for solving the reactive LES equations (1) is based on a central-upwind scheme from the Kurganov-Tadmor family, well-suited for compressible flows with strong discontinuities. Spatial discretization is performed using a finite volume approach, where numerical fluxes are computed via a flux-splitting technique that leverages local propagation speeds to ensure stability without requiring a full Riemann solver. Temporal integration is achieved through a second-order Runge-Kutta method, providing both accuracy and robustness. This scheme is conservative, non-oscillatory, and capable of accurately capturing shock waves and expansion fans, making it particularly effective for high-speed reactive flow simulations.

The combustion chemistry is integrated using a Rosebrock solver, [48]. The convective fluxes are reconstructed using the Kurganov central scheme, [49], whereas the diffusive fluxes are reconstructed using linear interpolation between neighbouring cells. The inviscid equations are solved explicitly whereas the viscous equations are solved iteratively using a Gauss Seidel smoother. With this numerical scheme, virtually linear scaling is achieved down to approximately 5000 cells per core.

5. Combustion Chemistry

Fuels with fast ignition properties are desired in high-speed combustion applications, and this may be even more critical under hypersonic conditions. Hydrogen (H_2) or small hydrocarbons such as ethylene (C_2H_4), are thus favourable candidates. Larger hydrocarbons, such as kerosene, do however have the advantage of high energy content per mass and ease of storage. Most research studies on high-speed combustion are performed using H_2 and that is also the fuel used in this work. Following [50-51] the choice of reaction mechanism is important for accurate LES predictions. It is therefore natural to study and scrutinize this aspect also for high-speed ramjet and scramjet combustion.

Figure 3 shows a comparison of experimental data and predictions from a set of H_2 reaction mechanisms for the laminar flame speed s_u, ignition time τ_{ign} and extinction strain rate σ_{ext}, for the mechanisms of Marinov (M1), [52], Eklund & Stouffer (ES7), [53], Baurle & Girimaji (BG7), [54], Davidenko et al. (D7), [55], Jachimovski (J20), [56], Alekseev et al. (K30), [57], Wang et al. (USCII), [58], and Zettervall &

Fureby, (Z22), [51]. For τ_{ign}, figure 3a, all mechanisms examined perform similarly at temperatures in excess of approximately 1000 K, but the Z22 mechanism appears the only one to reproduce τ_{ign} below 900 K. Concerning s_u, in figure 3b, M1 overpredicts s_u whereas ES7, BG7 and D7 all underpredicts s_u. J20, K30, USCII and Z22 all show good agreement with the experimental data. For σ_{ext}, figure 3c, M1 shows an overprediction whereas ES7, BG7 and D7 underpredict σ_{ext}. J20, K30, USCII and Z22 all show acceptable agreement with each other and with the experimental data, suggesting that these mechanisms can represent the effects of strain.

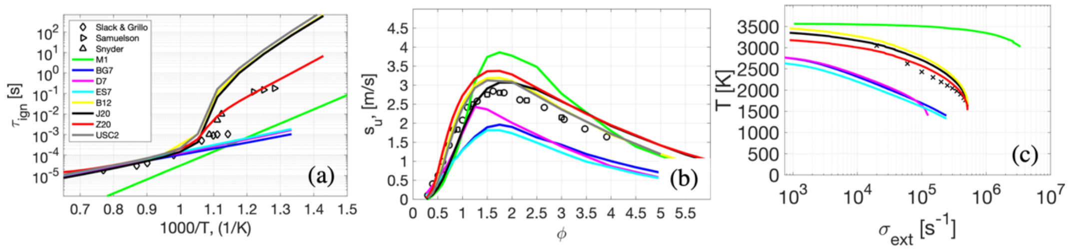

Fig. 3. Comparison of (a) laminar flame speed, s_u, (b) ignition delay time, τ_{ign}, and extinction strain rate, σ_{ext}, at 1 atm for H_2-air mixtures. Experimental data (symbols) from [59-61], [62-63], and [64].

6. Results

In this section we will compare simulation results for cases F1, F3 and F5 with each other and with experimental data from Fotia & Driscoll, [15-16], to enhance our understanding of the ramjet to scramjet transition and to further validate the LES model. The ramjet to scramjet transition is emulated by keeping the mass flow of air constant and reducing the equivalence ratio according to Table 1. This is of course different from the real transition process but allows us to compare predictions with experiments and draw conclusions from the combined results.

Figure 4 shows perspective views of the LES predictions of all three cases. The figure show contours of the refractive index gradient, ∇n, iso-surfaces of the second invariant of the velocity gradient, λ_2, (gray) and volumetric renderings of the H_2 mass-fraction (green) and the temperature, T, (warm colors). Based on ∇n we observe that the shock-train begins directly after the throat but then develops differently along the isolator depending on ϕ: For high values of ϕ (ramjet mode, case F1), the shock-train is short whereas for low values of ϕ (scramjet mode, case F5) the shock-train is longer. After this region the shock-train gradually disintegrates due to the combined effects of shock-boundary layer interaction, shock-shock interactions, and downstream volumetric expansion. As observed by comparing the ∇n distributions, the volumetric expansion increases with increasing ϕ and is higher in ramjet mode than in scramjet mode.

The vortical flow, characterized by coherent λ_2 structures, appears to be initiated simultaneously in the upper and lower boundary layers of the isolator just after the end of the shock-train. This behaviour suggests that the isolator boundary layer separates in this region, further enforcing the breakdown of the shock-train. The vortical flow then rapidly spreads across the full isolator cross-section, increasing the transverse mixing and widening the boundary layer. Just upstream of the cavity, H_2 is injected perpendicular to the main flow direction. This jet-in-cross flow configuration enhances both the transverse and spanwise mixing.

Downstream of the H_2 injection and along the cavity the coherent λ_2 flow structures are observed to decrease in size and increase in numbers and geometrical complexity. This is particularly evident in the cavity shear layers, which are shed from the cavity leading edge, and around the H_2 plume. The single-time snap shot of λ_2 appears chaotic, but averaging λ_2 reveals a horseshoe vortex pair sweeping around the H_2 jet plume and being slightly diverted down into the cavity before breaking up near the end of the cavity. On average, the H_2 plume itself consists of a counter-rotating vortex pair and ring-like vorticies surrounding the pair. In addition, boundary layer flow structures (longitudinal and hairpin vortices as well as streaks) also evolve after separation in the isolator, interacting with the plume vortex structures. Only small differences between λ_2 can be observed between the different cases, suggesting that λ_2 or the vorticity is subordinate to other quantities such as the flow velocity, pressure, temperature, heat-release, etc. The temperature distributions reveal some differences between cases F1, F3 and F5 depending on the value of ϕ. This is similar to the differences observed in ∇n and reveal a wider and more space-filling high-temperature plume for the ramjet case F1 compared with the scramjet case F5. The effective plume angle decreases as the isolator flow speed increases due to the change in volumetric expansion over the cavity. Moreover, we find in all cases that burning occurs in the cavity and along the borders of the H_2 plume.

Fig. 4. Perspective views of the flow in terms of the refraction index gradient, ∇n, the 2nd invariant of the velocity gradient, λ_2, (gray) and the H_2 mass-fraction (green), and the temperature, T, (warm colors) for (a) Case F1, (b) Case F3 and (c) Case F5.

To further understand and assess the flow physics involved in the transition between ramjet and scramjet modes associated with the experimental study of Fotia & Driscoll, [15-16], we compare volumetric renderings from the side of the instantaneous distributions of (from top to bottom) axial velocity, v_x, pressure, p, refractive index gradient, ∇n, temperature, T, heat release rate, Q, Takeno flame index, $TFI = (\nabla Y_{\mathrm{H2}} \cdot \nabla Y_{\mathrm{O}})/|\nabla Y_{\mathrm{H2}} \cdot \nabla Y_{\mathrm{O}}$, and species ($H_2$ in green and OH in orange) for cases F1, F3 and F5. By comparing the v_x-distributions we observe that a high-speed flow core develops just downstream of the contoured nozzle and penetrate into the isolator to different depths depending on the equivalence ratio, ϕ, with case F1 showing the smallest penetration and case F5 the deepest. The high-speed core ends abruptly, showing signs of boundary layer separation and shock disintegration. During the remaining part of the isolator the flow speed remains uniform until H_2 is injected.

When the H_2 is injected the lower boundary layer becomes distorted by the horseshoe vortex pair developing around the jet. The lower boundary layer then breaks up over the cavity, and a recirculation region is formed in the cavity. This recirculation region becomes stronger with increasing equivalence ratio. At the tapered end of the cavity the flow starts to accelerate, in particular above the cavity. A significant acceleration is then seen along the whole downstream combustor due to the volumetric expansion from the heat release. The pressure reveals a significant build-up over and in front of the cavity because of the volumetric expansion. The upstream extent of this depends on ϕ, with the longest for case F1 and the shortest for case F5.

The Schlieren or ∇n images show how the refractive index changes as a consequence of the longer v_x penetration and reduced heat release with decreasing ϕ from case F1 to F5. Note here that ∇n is influenced by the H_2 injection, the shock-train, as well as the volumetric expansion from heat-release. The temperature increases somewhat along the isolator as a consequence of the increase in pressure. The pressure rises because of the blockage caused by the expansion. After the H_2 injection a large increase in T is observed around the entire H_2 plume and in the cavity. The cavity acts as a flameholder since hot gases from the trailing edge of the cavity are recirculated towards the leading edge where it heats up the shear layer above the cavity. The shear layer then interacts both with the H_2 rich plume and the hot air from the isolator surrounding the plume. The heat release, Q, occurs mainly on the outer edges of the H_2 rich plume but to some extent also in the trailing edge of the cavity where fuel is entrained.

Q shows evidence of the vortical structures described in figure 4, including sheet-like elements on the outer edges of the H_2 rich plume and ring-shaped vorticies enclosing the H_2 rich plume.

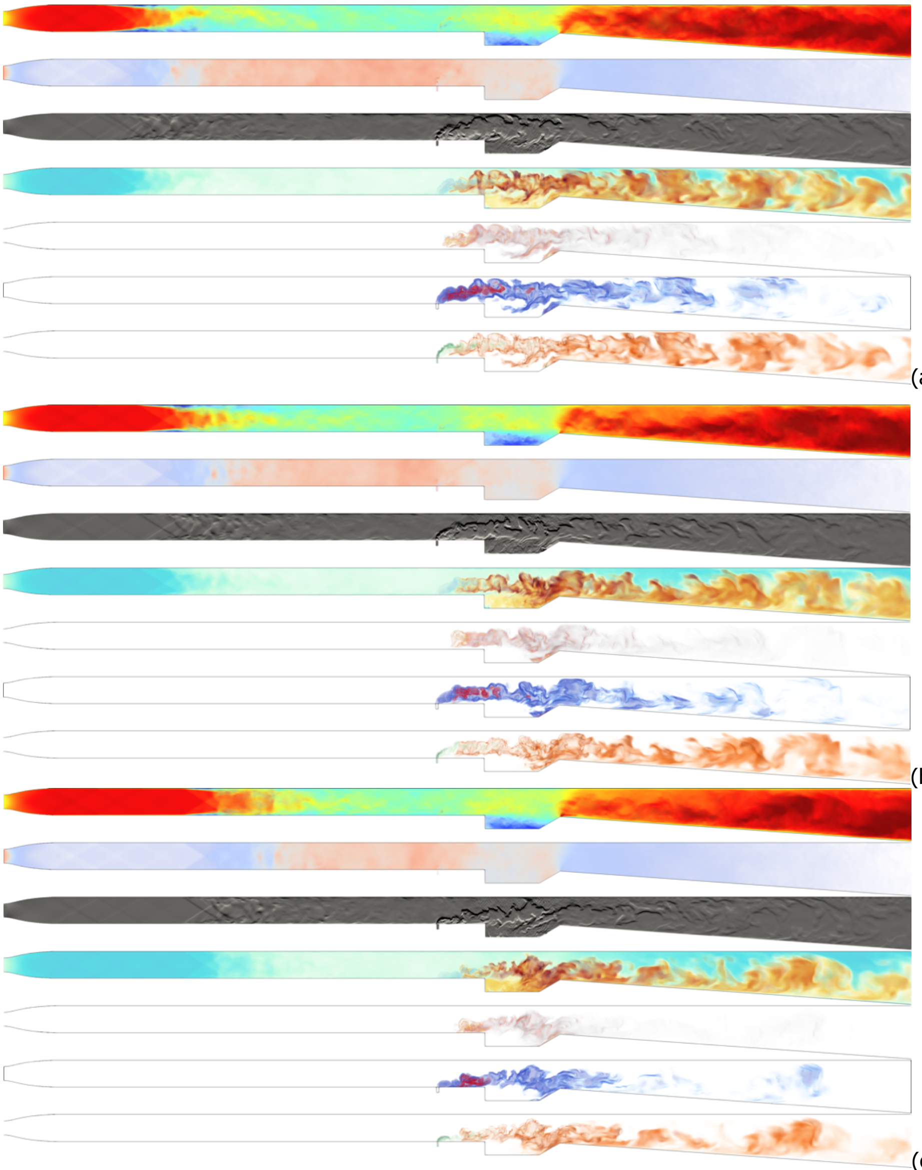

Fig. 5. Side-views of (top to bottom) axial velocity, v_x, pressure, p, refractive index gradient, ∇n, temperature, T, heat release rate, Q, Takeno flame index, TFI, and species (H_2 in green and OH in orange) for case (a) F1, (b) F3 and (c) F5.

The Takeno flame index reveals that the majority of the heat release takes place in non-premixed structures, defined by $\nabla Y_{H2} \cdot \nabla Y_{O2} < 0$ and shown in blue in figure 5. A smaller premixed core with $\nabla Y_{H2} \cdot \nabla Y_{O2} > 0$, shown in red, can also be observed. Finally, we compare the distributions of the species H_2 and hydroxide, OH. OH, typically occurs in thin and strongly wrinkled flames where the majority of heat release takes place, and OH is generally not overlapping with H_2. The shape of the heat release, Q, is virtually unaffected by ϕ, but the plume is pushed down, towards the lower wall, when ϕ is increased as the relative heat release decreases and the scramjet mode of operation is approached.

Figure 6 compares experimental shearing interferograms (top row) with corresponding images from the LES (bottom row). Shearing interferograms, [65], allow for the visualization of the phase difference between two beams of light due to the presence of a phase object, i.e. the combustor flow. Experimentally, the light was sheared in the flow parallel orientation to allow for the best visualization of the density gradients. The images shown in figure 6a to 6c are constructed by calculating the absolute gradient of the recorded intensity field, $\nabla^2 I$, where I is the light intensity. Numerically, the shearing interferograms are approximated, following, [62], by $\nabla^2 n$, providing a reasonable estimate. It is found that the trend of a gradually shallower combustion region from ramjet mode (case F1) to scramjet mode (case F5) is qualitatively captured but also that a number of details are not captured. These discrepancies are most likely to be the result of comparing two different quantities.

Fig. 6. Experimental shearing interferogram (top row) and numerical shadowgraph images (bottom row) of the combustor from the side for (a and d) case F1, (b and e) case F3, and (c and f) case F5.

Figure 7 compares time-averaged and rms wall pressures, $\langle p \rangle_{wall}$ and p_{wall}^{rms}, from experiment and LES. Angle brackets denote time averaging and the superscript 'rms' denote rms fluctuations. Pressure acts as a marker of the combustion dynamics in a thermally choked flow since any change in Q will result in a change in the shock-train and pressure rise. Reasonable agreement between LES and experimental data is found for $\langle p \rangle_{wall}$, particularly for the trends associated with ϕ and the transition from ramjet to scramjet mode. The computed profiles of $\langle p \rangle_{wall}$ show a steeper rise halfway through the isolator than the experimental data but do reach the expected levels before and within the cavity. At the downstream edge of the cavity and in the first part of the combustor good agreement with the experimental data is observed. The differences between LES and experiments increase with decreasing ϕ, suggesting that the scramjet case F5 is burning somewhat too quickly. The peak of p_{wall}^{rms} occurs in the isolator due to the breakdown of the shock-train. Based on p_{wall}^{rms} the ramjet case F1 is the steadiest since the reaction-zone is mainly located in the low-speed upstream part of the cavity shear-layer. The scramjet case F5 is the least steady as the reaction zone is moved further downstream in the shear layer. The intermediates case F3, representing transition, appears between the ramjet and scramjet cases.

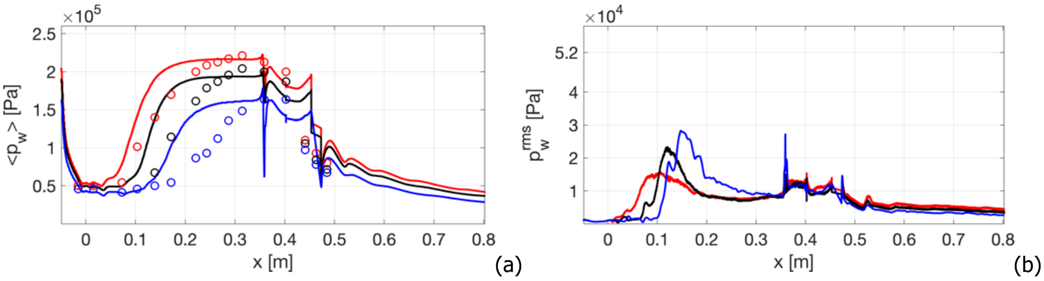

Fig. 7. Time-averaged wall pressure (a) and rms wall pressure fluctuations (b) along the lower combustor-wall from experiments, [E1-E2], and the present LES. Legend: Experimental data for case F1 (○), case F3 (○) and case F5 (○), and LES results for case F1 (—), case F3 (—) and case F5 (—).

Figure 8 presents some key 1D metrics for assessing the overall performance of the isolator-combustor configuration. In figure 8a we present the heat release, Q, which peaks just downstream of the fuel injector for all cases, but most apparently in the ramjet and transitional cases F1 and F3. In the scramjet case F5, combustion appears more distributed along the cavity with a much smaller initial peak. After the cavity Q rapidly decrease in the first part of the combustor. In figure 8b we show the cross-section averaged density-weighted Ma number. For all cases considered, Ma peaks at ~2 in the nozzle, which is close to the design Ma number of 2.2. This suggests that the nozzle flow agrees well with the experimental setup and the reference data. In the isolator, Ma decreases down to values between 0.5 to 0.6 depending on the case, with the lower Ma number corresponding to the ramjet case and the higher Ma number to the scramjet case. Ma starts to increase along the tapered part of the cavity and along the combustor following the volumetric expansion due to combustion. Similarly, in figure 8c we show cross-section averaged normalized streamthrust, s/s_{nozzle}, in which $s = \int_C (p + 0.5\rho v^2)\, \rho dA / \int_C \rho dA$ where C is the cross-section. Here, s slowly increases along the isolator, with some differences between cases associated with the different longitudinal evolution of the shock-train and the amount of heat release and volumetric expansion produced by the combustion. At the fuel injection location s increases again, and in the cavity s increases yet again, after which it decreases to a level somewhat above that in the isolator. Figure 8d shows the fuel conversion factor (i.e. combustion efficiency) defined as $\eta = 1 - \int_C Y_{H2}\,\rho v_x\, dA / \int_C Z_H \rho v_x\, dA$ where Z_H is the mass fraction of all H atoms. The ramjet case takes longer distance to consume the fuel but there is also more fuel injected in this case. In the end, more than 95% of the injected fuel is consumed in all of the three cases considered.

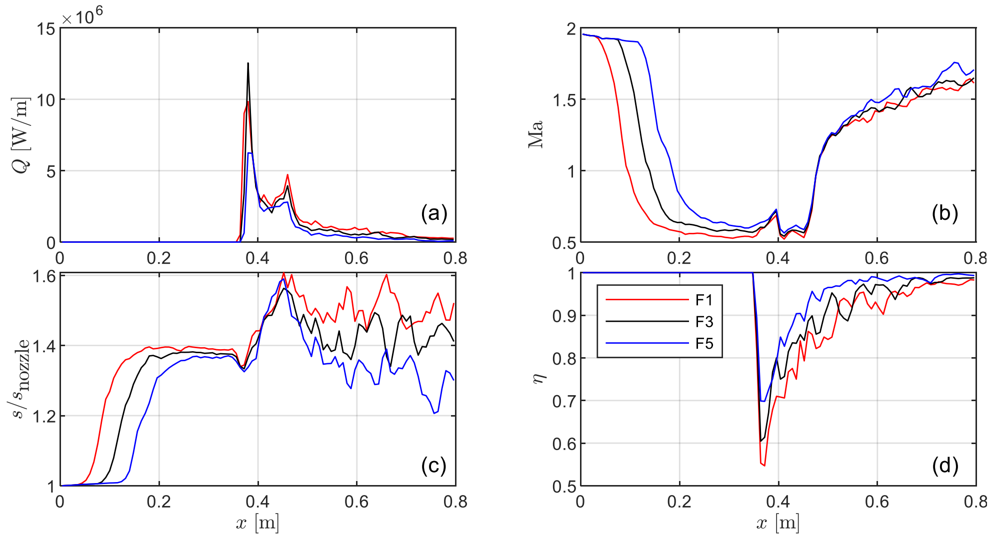

Fig. 8. (a) Heat release, Q, (b) Mach number, Ma, (c) normalized streamthrust, s/s_{nozzle}, and (d) conversion factor or combustion efficiency, η, for cases F1, F3 and F5.

Figure 9 shows the accumulated heat release as a percentage as function of equivalence ratio ϕ and flame index, TFI. From these panels it is seen that ~70 % of heat is released in lean regions and ~75 % is released in non-premixed regions with $TFI < 0$. A strong bias is seen for the purely non-premixed regions hinting that the combustion is primarily limited by mixing as would be expected. This is also clearly observed in figure 5, where non-premixed combustion dominates but where premixed combustion occurs in parts of the jet plume. As already seen in figure 5, and quantified here, the lean and non-premixed combustion dominate in all cases.

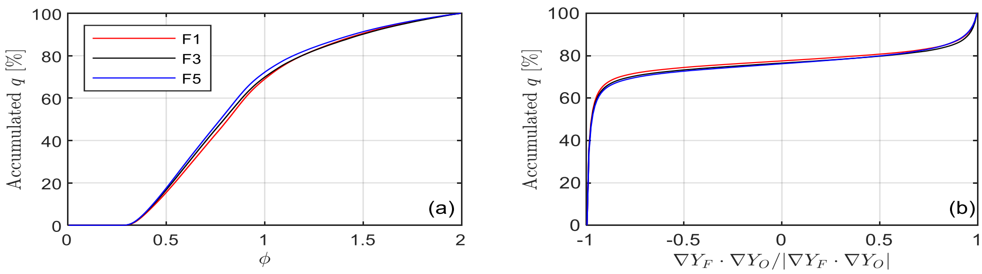

Fig. 9. Accumulated heat released as function of (a) equivalence ratio and (b) TFI.

7. Concluding Remarks

Here, finite rate chemistry Large Eddy Simulation (LES) was used to investigate flow, mixing, self-ignition and cavity stabilized turbulent combustion in the University of Michigan laboratory dual-mode ramjet combustor. The conditions corresponded to stagnation temperatures and pressures of T_0= 1400 K and of p_0=448.2 kPa, respectively. Varying equivalence ratios, ϕ, are used to emulate the transition from ramjet mode at ϕ=0.34 to scramjet mode at ϕ=0.19. By comparing the LES predictions with the experimental data in terms of shearing interferogram images and numerical shadowgraph images, respectively, and wall-pressure data we conclude that the LES results agree qualitatively well with the experimental data, capturing the transition process. However, the LES overpredicts the wall-pressure, suggesting that also the volumetric expansion and the heat release are overpredicted. The reason for that seems to be that the reaction mechanisms predict somewhat too early ignition under the particular conditions studied here. The fact that the transition process is qualitatively captured can be used to elucidate the flow and combustion processes in ramjet, transition and scramjet modes.

Ramjet combustion occurs for high equivalence ratios, where the supersonic isolator flow is terminated by a normal shock or a very rapid shock breakdown. The fuel injection and subsequent combustion results in a large volumetric expansion and pressure increase that propagates upstream to balance the rapid isolator shock breakdown. Scramjet combustion occurs for low equivalence ratios, where the supersonic isolator flow is longer and is terminated by a more gradual shock breakdown. The fuel injection and combustion results in a volumetric expansion and high pressure that propagates upstream to balance the isolator shock breakdown. The transition between these bracketing modes, represented by case F3, appears to be a gradually developing process dominated by the gradual change of the balance between the shock breakdown and the pressure build-up due to volumetric expansion caused by the combustion induced heat-release. Lean and non-premixed combustion dominates for the entire transition.

The behaviour of a supersonic isolator coupled to a combustor is a complex and fully coupled system. Understanding the interactions between the flame, the geometry, and pressure field with its subsequently formed shocks is critical if high-speed air-breathing propulsion technology is to be tamed.

Acknowledgement

The author acknowledges the many interesting discussions with Prof. Driscoll. Computational resources were provided by the National Academic Infrastructure for Supercomputing in Sweden (NAISS), partially funded by the Swedish Research Council through grant agreement no. 2022-06725.

References

[1] Andreadis D., 2004, "Scramjet Engines Enabling the Seamless Integration of Air and Space Operations", The Industrial Physicist, 10, p 24.
[2] Fry R.S.; 2004, "A Century of Ramjet Propulsion Technology Evolution", J. Prop. Power, 20. p 27.
[3] Urzay J.; 2018, "Supersonic Combustion in Air Breathing Propulsion Systems for Hypersonic Flight", Annual Rev. Fluid Mech., 50, p 593.
[5] Gonzalez-Juez E.D., Kerstein A.R., Ranjan R. & Menon S.; 2017, "Advances and challenges in modeling high-speed turbulent combustion in propulsion systems", Prog. Energy Comb. Sci., 60, p 26.
[6] Trefny C.J. & Benson T.J.; 1995, "An Integration of the Turbojet and Single-Throat Ramjet", NASA Technical Memorandum 107085.
[7] Huang W., Da Z.-B., Yan L. & Moradi R.; 2018, "Flame Propagation and Stabilization in Dual-Mode Scramjet Combustors: A Survey", Prog. Aerospace Sci., 101, p 13.
[8] Fureby C.; 2021, "Supersonic Combustion Physics – A Grand Challenge for Numerical Modeling", Stratospheric Flying Opportunities for High-Speed Propulsion Concepts, von Karman Institute Lecture Series, May 26.
[9] Fotia M.L. & Driscoll J.F.; 2012, "Isolator–Combustor Interactions in a Direct-Connect Ramjet-Scramjet Experiment", J. Prop. Power, **28**, p 83.
[10] Fotia M.L. & Driscoll J.F.; 2013, "Ram-Scram Transition and Flame/Shock-Train Interactions in a Model Scramjet Experiment", J. Prop. Power, **29**, p 261.
[11] Liu J., Yuan H., Hua Z., Chen W. & Ge N.; 2017, "Experimental and Numerical Investigation of Smooth Turbine-based Combined-Cycle Inlet Mode Transition", Aerospace Science and Tech., 60, p 124.
[12] Wang D., Cai Y.H., Song W.Y. & Xiao Y.L.; 2007, "Numerical Research on Subsonic-Combustion and Supersonic-Combustion Modes in Scramjet Chamber", J. Solid Rocket Tech., 30, p. 26.
[13] Micka D.J. & Driscoll J.F.; 2009, "Combustion Characteristics of a Dual-Mode Scramjet Combustor with Cavity Flameholder", Proc. Comb. Inst., 32, p 2397.
[14] Wang Z.G., Wang H.B. & Sun M.B.; 2014, "Review of Cavity-Stabilized Combustion for Scramjet Applications", Proc. Inst. Mech. Eng., Part G J. Aerosp. Eng., 218, p 2718
[15] Fotia M.L. & Driscoll J.F.; 2012, "Isolator–Combustor Interactions in a Direct-Connect Ramjet-Scramjet Experiment", J. Prop. Power, **28**, p 83.
[16] Fotia M.L. & Driscoll J.F.; 2013, "Ram-Scram Transition and Flame/Shock-Train Interactions in a Model Scramjet Experiment", J. Prop. Power, **29**, p 261.
[17] Zettervall N. & Fureby C.; 2018, "A Computational Study of Ramjet, Scramjet and Dual- Mode Ramjet/Scramjet Combustion in a Combustor with a Cavity Flameholder" AIAA 2018-1146.

[18] Nilsson T., Zhong S. & Fureby C.; 2021, "LES of H_2-air Jet Combustion in High Enthalpy Supersonic Crossflow", Phys. Fluids, **33**, 035133.
[19] Celik I., Cehreli Z. N., & Yavuz I.; 2005, "Index of Resolution Quality for Large Eddy Simulations", ASME, J. Fluids Engineering, 127, p 949.
[20] Fureby C. 2015, "Challenges of Large Eddy Simulations of Engineering Flows", in Whither Turbulence and Big Data for the 21st Century, Ed. Pollard A., p 375. Springer Verlag.
[21] Menon S. & Fureby C.; 2010, "Computational Combustion", In Encyclopedia of Aerospace Engineering, Eds. Blockley R. & Shyy W., John Wiley & Sons.
[22] Echekki T. & Mastorakos E.; 2011 (Eds.), "Turbulent Combustion Modeling", Fluid Mechanics and its Ap-plications, 95, Springer Science+Business Media.
[23] Giacomazzi E., Picchia F.R. & Arcidiacono N.; 2007, "On the Distribution of Lewis and Schmidt Numbers in Turbulent Flames", 30th Event of the Italian Section of the Combustion Institute
[24] Sagaut P.; 2001, "Large Eddy Simulation for Incompressible Flows", Springer Verlag.
[25] Li Y., Chevillard L., Eyink G. & Meneveau C.; 2009, "Matrix Exponential-based Closures for the Turbulent Subgrid-scale Stress Tensor", Phys Rev. E, 79 p 016305
[26] Erlebasher G., Hussaini M., Special C. & Sang T.; 1992, "Towards the Large Eddy Simulation of Compressible Turbulent Flows", J. Fluid Mech., **238**, p 155.
[27] Nicoud F. & Ducros F.; 1999, "Subgrid-Scale Stress Modelling Based on the Square of the Velocity Gradient Tensor", Flow, Turb. and Comb., **62**, p 183.
[28] Cook A.W. & Cabot W.H.; 2005, "Hyperviscosity for Shock-Turbulence Interactions". J. Comp. Phys., **203**, p 379.
[29] Kim W.-W. & Menon S.; 1995, "A New Dynamic One Equation Subgrid-scale Model for Large Eddy Simu- lations", AIAA 95-0356.
[30] Fureby C.; 2021, "Subgrid Models, Reaction Mechanisms and Combustion Models in LES of Supersonic Combustion", AIAA J., **59**, p 215.
[31] Cook A.W. & Riley J.J.; 1994, "A Subgrid Model for Equilibrium Chemistry in Turbulent Flows", Phys. Fluids, **6**, p 2868.
[32] Hawkes E.R. & Cant R.S.; 2001, "Implications of a Flame Surface Density Approach to Large Eddy Simulation of Premixed Turbulent Combustion", Comb. Flame, **126**, p 1617.
[33] Colin O., Ducros F., Veynante D. & Poinsot T.; 2000, "A Thickened Flame Model for Large Eddy Simulation of Turbulent Premixed Combustion", Phys. Fluids., **12**, p 1843.
[34] Fureby C.; 2009, "LES Modeling of Combustion for Propulsion Applications", Phil. Trans. R. Soc. A, **367**, p 2957.
[35] Sabelnikov V. & Fureby C.; 2013, "LES Combustion Modeling for High Re Flames using a Multi-phase Analogy", Comb. Flame, **160**, p 83.
[36] Giacomazzi E., Bruno C. & Favini B.; 2000, "Fractal Modeling of Turbulent Combustion", Comb. Theory & Modeling, **4**. p 391.
[37] Batchelor G.K. & Townsend A.A.; 1949, "The Nature of Turbulent Motion at Large Wave-numbers", Proc. Roy. Soc. London A, **199**, p 238.
[38] Chomiak J.; 1970, "A Possible Propagation Mechanism of Turbulent Flames at High Reynolds Numbers", Comb. Flame, **15**. p 319.
[39] Jones W.P., Marquis A-J. & Wang F.; 2015, "Large Eddy Simulation of a Premixed Propane Turbulent Bluff Body Flame using the Eulerian Stochastic Field Method", Fuel, **140**, p 514.
[40] Gao F. & O'Brian E.; 1993, "A Large Eddy Simulation Scheme for Turbulent Reacting Flows", Phys Fluids A, **5**, p 1282.
[41] Menon S., 2000, "Subgrid Combustion Modeling for Large Eddy Simulations", Int. J. Engine Res., **1**, p 209.
[42] Fureby C., Zettervall N., Kim S. & Menon S.; 2015, "Large Eddy Simulation of a Simplified Lean Premixed Gas Turbine Combustor", 9th Int. Symp. on Turbulence and Shear Flow Phenomena (TSFP-9), Melbourne, Aus.
[43] Fedina E., Fureby C., Bulat G. & Maier W.; 2017, "Assessment of Finite Rate Chemistry Large Eddy Simulation Combustion Models", Flow, Turb. and Comb., **99**, p 385.
[44] Fureby C.; 2018, "The Volvo Validation Rig – A Comparative Study of Large Eddy Simulation Combustion Models at Different Operating Conditions", AIAA 2018-0149.
[45] Tanahashi M., Fujimura M. & Miyauchi T.; 2000, "Coherent Fine Scale Eddies in Turbulent Premixed Flames", Proc. Comb. Inst. 28, p 5729.
[46] Kawai S. & Lele S.K.; 2008, "Localized Artificial Diffusivity Scheme for Discontinuity Capturing on Curvilinear Meshes," J. Comp. Phys., **227**, p 9498.

[47] Adams N.A. & Shariff K.; 1996, "A High-Resolution Hybrid Compact-ENO Scheme for Shock-Turbulence Interaction Problems," Journal of Computational Physics, **127**, p 27.
[48] Hairer E. & Wanner G.; 1991, "Solving Ordinary Differential Equations", II: Stiff and Differential-Algebraic Problems, 2nd Ed., Springer Verlag.
[49] Kurgaonov A., Noelle S., Petrova G.; 2001, "Semidiscrete Central Upwind Schemes for Hyperbolic Conservation Laws and Hamilton Jacobi Equations", SIAM J. Sci. Comp., **23**, p 707.
[50] Fedina E., Fureby C., Bulat G. & Maier W.; 2017, "Assessment of Finite Rate Chemistry Large Eddy Simulation Combustion Models", Flow, Turb. and Comb., **99**, p 385.
[51] Zettervall N. & Fureby C.; 2018, "A Computational Study of Ramjet, Scramjet and Dual-mode Ramjet Combustion in Combustor with a Cavity Flameholder", AIAA 2018-1146.
[52] Marinov N.M., Westbrook C.K. & Pitz W.J.; 1995, "Detailed and Global Chemical Kinetics Model for Hydrogen", 8th Int. Symp. on Transport Properties, San Francisco, CA, USA.
[53] Eklund D.R. & Stouffer S.D.; 1994, "A Numerical and Experimental Study of a Supersonic Combustor Employing Swept Ramp Fuel Injectors", AIAA 94-2819.
[54] Baurle R.A. & Girimaji S.S.; 2003, "Assumed PDF Turbulence-Chemistry Closure with Temperature Com-position Correlations", Comb. Flame, **134**, p. 131.
[55] Davidenko D.M., Gökalp I., Dufour E. & Magre P.; 2003, "Numerical Simulation of Hydrogen Supersonic Combustion and Validation of Computational Approach", AIAA 2003-7003.
[56] Jachimowski C.J.; 1988, "An Analytical Study of the Hydrogen–air Reaction Mechanism with Application to Scramjet Combustion", NASA-TP-2791.
[57] Alekseev V.A., Christensen M. & Konnov A.A.; 2015, "The Effect of Temperature on the Adiabatic Burning Velocities of Diluted Hydrogen Flames: A Kinetic Study using an Updated Mechanism", Comb. Flame, **162**, p. 1884.
[58] Wang H., You X., Joshi A.V., Davis S.G., Laskin A., Egolfopoulos F. & Law C.K.; 2007, "USC Mech. Ver-sion II. High-Temperature Combustion Reaction Model of H2/CO/C1-C4 Compounds", Mechanism and additional information is available at http://ignis.usc.edu/USC_Mech_II.htm.
[59] Slack M. & Grillo A.; 1977, "Investigation of Hydrogen-Air Ignition Sensitized by Nitric Oxide and by Nitrogen Oxide", NASA Report CR-2896.
[60] Samuelsen S., McDonell V., Greene M. & Beerer D.; 2006, "Correlation of Ignition Delay with Natural Gas and IGCC type Fuels", 2006, DOE Award Number: DE-FC26-02NT41431.
[61] Snyder A.D., Robertson J., Zanders D.L. & Skinner G.B.; 1965, "Shock Tube Studies of Fuel-Air Ignition Characteristics", Report AFAPL-TR-65-93-1965
[62] Kwon O.C. & Faeth G.M.; 2001, "Flame/Stretch Interactions of Premixed Hydrogen-Fueled Flames: Measurements and Predictions", Comb. Flame, **124**, p 590.
[63] Dowdy D.R., Smith D.B., Taylor S.C. & Williams A.; 1990, "The Use of Expanding Spherical Flames to Determine Burning Velocities and Stretch Effects in Hydrogen-Air Mixtures", Proc. Comb. Inst., **23**, p 325.
[64] Juniper M., Darabiha N. & Candel S.; 2003, "The Extinction Limits of a Hydrogen Counterflow Diffusion Flame above Liquid Oxygen", Comb. & Flame, **135**, p 87.
[65] Merzkirch W.; 1974, "Generalized Analysis of Shearing Interferometers as Applied for Gas Dynamics Studies", J. Appl. Optics, 13, p 409.
[62] Falldorf C. & Bergman R.B.; 2013, "Wave Field Sensing by Means of Computational Shear Interferometry", J. Opt. Soc. America, 30, p 1905.